

Hydrophobic Waxes in Ivory Nuts Affect Surface Modification by Atmospheric Air Plasma Jet

Yuri Ferreira da Silva ¹ , Renata Nunes Oliveira ² , Renata Antoun Simao ^{1,*} 

¹ Department of Metallurgical and Materials Engineering, Federal University of Rio de Janeiro, P.O. Box: 68505, 21945-970, Rio de Janeiro, RJ, Brazil; yuri@metalmat.ufrj.br (Y.F.S.); renata@metalmat.ufrj.br (R.A.S.);

² Department of Materials Engineering, Federal Rural University of Rio de Janeiro, Km 7 BR 465, 23890-000, Seropédica, RJ, Brazil; renatanunes.ufrj@gmail.com (R.A.S.);

* Correspondence: renata@metalmat.ufrj.br;

Scopus Author ID 54933069800

Received: 15.11.2020; Revised: 22.12.2020; Accepted: 28.12.2020; Published: 3.01.2021

Abstract: Ivory nuts, bioproducts from South American palms, possess a hard, water-insoluble, and microporous endosperm with a strong resemblance to elephant ivory. The nuts sustainable appeal made them popular as eco-friendly substitutes to ivory and, more recently, microbeads. However, their hygroscopicity and mannan composition impart susceptibility to deterioration by microbes and insects. Cold plasma treatment has been widely investigated as a clean and cost-effective procedure for seed disinfection and surface modification. Hence, in this work, ivory nut endosperm was treated by an air plasma jet to modify wettability. Plasma treated samples were characterized by the water contact angle, AFM, and Raman imaging. Water contact angle results presented an increase from $(31.5 \pm 8.7)^\circ$ to $(78.9 \pm 5.4)^\circ$, demonstrating surface hydrophobization. This result was attributed to the modification of surface chemistry by migration and repolymerization of extractives promoted by plasma treatment. AFM results evidenced the formation of a heterogeneous layer containing lamellar features similar to plant epicuticular waxes. Besides, principal component analysis of Raman imaging results highlighted spectral contributions from wax, xylan, mannan, and lignin. These results demonstrate that atmospheric air plasma jets can be employed for ivory nut hydrophobization with no need for additional precursors, altering surface chemistry by crosslinking endosperm native substances.

Keywords: ivory nut; phytelephas; mannan; xylan; epicuticular wax; plasma jet; water contact angle; AFM imaging; Raman imaging; principal component analysis.

© 2020 by the authors. This article is an open-access article distributed under the terms and conditions of the Creative Commons Attribution (CC BY) license (<https://creativecommons.org/licenses/by/4.0/>).

1. Introduction

The search for eco-friendly options for synthetic non-biodegradable polymers has redrawn the attention to bioproducts [1–5]. For instance, ivory nuts, Amazonian seeds once notorious as a resource for the manufacture of buttons before World War II [6,7], have been commercialized recently as a substitute to microbeads employed in personal care products, e.g., lotions and exfoliators [8,9]. These seeds present a relatively hard and water-insoluble endosperm (Figure 1) with an ivory-like color, making them popular in the handcrafts industry as a green alternative to animal ivory [10–12]. This bioproduct is produced by South American palms found in countries such as Brazil, Ecuador, and Colombia. It benefits traditional forest communities economically without promoting deforestation or animal poaching [6,13].

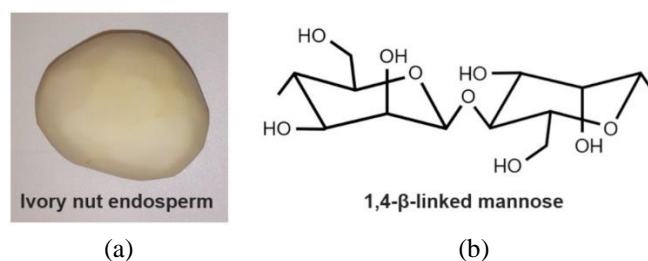


Figure 1. (a) Ivory nut endosperm after seed coat removal; (b) 1,4-β-linked mannose repeating units.

However, their biodegradability, an advantage compared to synthetic polymers, makes them vulnerable to deterioration by fungi, bacteria, and insects [14–16]. As illustrated in Figure 1, their endosperm's main constituent is pure mannan, a polysaccharide formed by β-1,4-linked mannose residues with a low degree of substitution by other monosaccharides, e.g., glucose and galactose [17–19]. This polysaccharide accounts for approximately 80 % of the endosperm total weight [17]. Similar to cellulose, mannan molecules are abundant in hydroxyl (-OH) functionalities, contributing to hygroscopic behavior [15]. Besides, the endosperm presents a network of tubules with micrometric dimensions [10] that may facilitate water retention, making the material a favorable environment for pathogen development.

Hence, to ensure ivory nut durability and commercial relevance, a cost-effective procedure is required for seed disinfection and hygroscopicity reduction. In this context, cold plasmas stand out as viable solutions. They can be generated near room temperature, allowing modification of substrates sensitive to high temperatures, such as seeds [20–22]. In addition to that, the modification promoted by plasma is restricted to external material layers, providing novel characteristics to surfaces without affecting substrate fundamental properties. Moreover, plasma processing is considered eco-friendly compared to techniques based on chemical agents. It is a solvent-free process that requires limited usage of precursors [23,24].

Cold plasmas have been widely investigated as a postharvest procedure for agricultural seeds. They can provide disinfection and modify surface chemistry, increasing wettability and enhancing germination rate [20,21,25]. In particular, plasma treatment systems at atmospheric pressures have attracted attention lately since they do not require vacuum equipment, increasing cost-effectiveness and facilitating their association with industrial processes [26–28]. One of the most frequent atmospheric pressure plasma sources is plasma jets. A feed gas flows between concentric electrodes. The generated plasma discharge is ejected towards the substrate, performing the treatment in open air [23,29]. During operation, a plasma jet system is shown in Figure 2, in addition to a schematic diagram of system configuration.

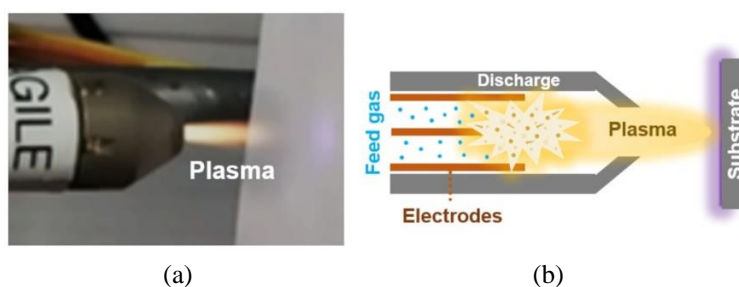


Figure 2. (a) Plasma jet (Plasma Pen™, PVA TePla America, USA) during operation. (b) Schematic diagram of plasma jet configuration for discharge generation and substrate treatment.

In this work, ivory nut endosperm was treated by a cold plasma jet fed with ambient air. In general, air plasma treatments result in increased hydrophilicity as a result of a surface

etching by plasma energetic species and interaction with reactive oxygen species (ROS) or reactive nitrogen species (RNS), such as hydroxyl radicals and nitric oxide (NO), respectively [30–34]. Nevertheless, air plasma jet treatment of ivory nut endosperm resulted in a considerable increase in hydrophobicity observed by water contact angle measurements. Therefore, atomic force microscopy (AFM) and Raman imaging were employed to investigate the surface characteristics and chemical moieties associated with this wettability modification.

2. Materials and Methods

Ivory nut endosperm (SisGen Code: AC591E1) was cut into disk-shaped samples of approximately 0.5 cm in diameter. The sample surface was sanded with 100, 220, 400, and 600-grain sandpaper and posteriorly polished with alumina. After polishing, samples were thoroughly rinsed and cleaned in an ultrasound bath for 15 min. Lastly, ivory nut disks were stored in a desiccator for at least 24 h before processing and characterization.

Surface treatment was performed with an atmospheric pressure plasma jet (Plasma Pen™, PVA TePla America, USA) supplied with ambient air compressed at 7 bar. The samples were kept at a 1.5 cm distance from the plasma nozzle to perform treatment in the afterglow region and avoid overheating. The sample surface was scanned by the plasma jet for 80 s at a 1.36 cm/s speed with an automatic motion system built using an Arduino microcontroller and stepper motors from CD / DVD drives. Detailed information on this setup is described elsewhere [11]. After treatment, samples were stored in a desiccator for 24 h before further characterization.

Static water contact angle measurements were performed in a Ramé-Hart 500 F1 goniometer. Droplets of distilled water ($\sim 5 \mu\text{L}$) were deposited on the sample surface, and 100 measurements were recorded with a 0.2 s interval. These measurements were performed in duplicate for each sample replicate ($n = 3$). Moreover, a JPK Nanowizard microscope was employed for obtaining surface topography and phase-contrast images in intermittent contact mode.

Raman spectra in 1000 to 1750 cm^{-1} region were obtained in a Witec Alpha 300 spectrometer. Single spectra were acquired using a 785 nm laser with a 0.5 s integration time and 200 accumulations. Hyperspectral imaging maps were acquired in a grid of 100 x 100 points located on a 20 x 20 μm^2 region. Spectral preprocessing steps consisted of background subtraction, cosmic ray removal, smoothing by Savitzky-Golay filter, and normalization by Standard Normal Variate (SNV) method. Further, linear baseline correction was performed. These preprocessing procedures were performed in Witec Project 2.10 software and Rstudio, employing the *hyperSpec* package [26].

Finally, principal component analysis (PCA) of Raman imaging data was executed in RStudio, with function *prcomp*. Plotting of results was performed through average score intensity maps and loading plots for the first four principal components. This methodology was based on work from Bonifacio *et al.* (2010) [36].

3. Results and Discussion

3.1. Surface wettability.

Static water contact angle results are shown in Figure 3. Plasma treatment promoted an increase in water contact angle from $(31.5 \pm 8.7)^\circ$ to $(78.9 \pm 5.4)^\circ$, indicating the incorporation of hydrophobic moieties to the sample surface. As the plasma jet was fed with atmospheric air,

the discharge is expected to be abundant in reactive nitrogen species (RNS). Reactive oxygen species (ROS) generated upon collisional processes with the accelerated electrons [30,37]. Moreover, as the treatment was performed in the open air, plasma discharge may interact with water vapor and generate hydroxyl (-OH) radicals [30]. Upon interaction with these species, an increase in polar surface character is expected, attributed to incorporating oxygen-containing functional groups [31]. However, the current results indicated surface hydrophobization.

Similar behavior was observed for atmospheric plasma treatment of wood. Black spruce (*Picea mariana*) samples treated by N₂ / O₂ plasma and sugar maple (*Acer saccharum*) treated by Ar / O₂ and CO₂ / N₂ plasmas presented water contact angles up to 120 °C, which were attributed to structural alterations and chemical rearrangement of constituents promoted by interaction with plasma-activated species [38]. Hydrophobization of wood surfaces has also been observed after thermal treatments. Wood drying at a temperature interval of 160-180 °C has promoted increases in surface hydrophobicity owing to the migration of extractives and other volatile substances towards the sample surface [39].

Based on these studies, the hydrophobicity observed for ivory nut endosperm surface after air plasma treatment may be caused by modification of cell wall constituents or migration of low molecular weight compounds, such as extractives, and further crosslinking at the surface. To further investigate surface alterations imparted by plasma treatment, the sample surface was analyzed by atomic force microscopy.

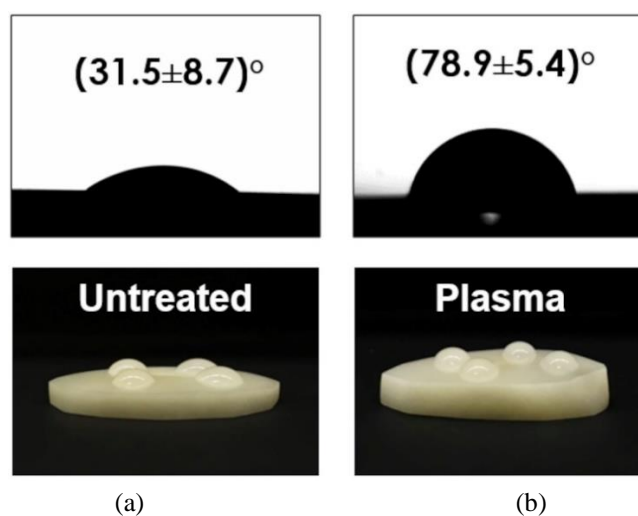


Figure 3. (a) Static water contact angle results for untreated ivory nut disk and sample treated by air plasma jet for 80 s. (b) Water drops on the sample surface to illustrate wetting behavior.

3.2. Atomic force microscopy.

AFM images for a $5 \times 5 \mu\text{m}^2$ region of untreated ivory nut sample are presented in Figure 4. The topography image shows that the surface presents a relatively rough aspect with granular submicrometric features. The phase-contrast image shows a stiffer phase embedded in softer material, represented by darker and lighter colors, respectively. Ivory nut endosperm cell walls have been reported to be constituted by distinct mannan polymorphs, mannan I and mannan II, associated with cellulose. Mannan I presents a higher degree of crystallization than mannan II and is present in cell walls in granular form, while mannan II is semicrystalline and may be associated with cellulose microfibrils [18,40]. Hence, the granular and stiffer material observed in Figure 4 may correspond to mannan I, which is respectively cemented by less

crystalline constituents such as mannan II and cellulose, presented in a lighter color in the phase-contrast image. These results demonstrate the granular and heterogeneous component distribution on the ivory nut endosperm surface.

In turn, these features were altered for the plasma-treated sample. The topography image shows that the treated sample presents a lower roughness in comparison to the untreated endosperm, indicating the formation of a more continuous layer on the surface, in contrast to the granular topography attributed to mannan I. Moreover, lamellar features with submicrometric dimensions could be observed. These elements are similar to platelet-shaped epicuticular wax crystals observed on pitcher plants' surface (*Nepenthes alata*). Epicuticular waxes form a rough and hydrophobic layer on plant surfaces and may hinder insect attachment due to slippery behavior [41]. Besides, phase contrast images also evidence the presence of lamellar softer regions forming a micrometric network structure among stiffer constituents.

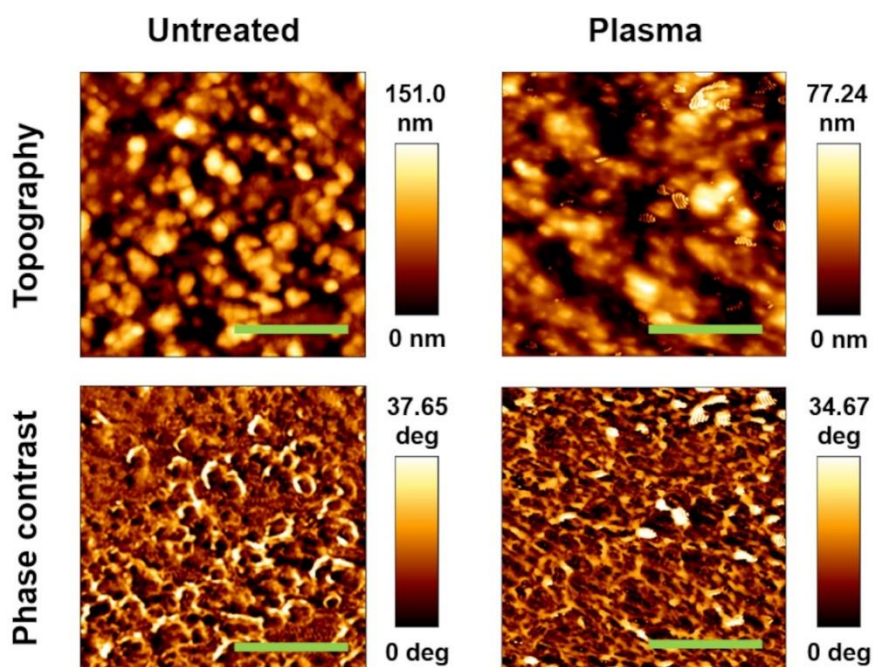


Figure 4. AFM topography and phase-contrast images for a $5 \times 5 \mu\text{m}^2$ region of untreated and plasma-treated ivory nut samples. Scale bars (green) = $2 \mu\text{m}$.

Wax features could not be observed at the untreated sample surface, indicating that plasma treatment may have promoted an enrichment of these substances at endosperm external layers. As the endosperm presents a porous microstructure, hydrophobic waxes could be initially present on pore walls and, upon bombardment by energetic plasma species, may be fragmented, migrate towards the surface and suffer crosslinking, forming the structure observed in a phase-contrast image. This assumption was based on the previous reports for wood cell walls [38,39]. In turn, the darker regions could correspond to cell wall polysaccharides, probably present in the endosperm pores as reserve substances. Further, Raman imaging of treated samples was performed to investigate chemical alterations promoted by plasma treatment.

3.3. Raman imaging of plasma-treated ivory nut endosperm.

Raman imaging was performed in a $20 \times 20 \mu\text{m}^2$ region located away from the endosperm pores, as shown in Figure 5, which also contains an average intensity map for the

obtained spectra. This image is constituted by a grid of 100 x 100 points, where each point corresponds to a single Raman spectrum. Thus, according to the image scale, points colored in red correspond to spectra with a higher average signal, while the ones colored in blue may present a lower intensity. Nevertheless, Raman spectra of plant cell walls usually present strong contributions from background signals generated by fluorescent constituents [42,43]; thus, the distinct regions present in Figure 5 may be associated with a higher concentration of fluorescent substances, e.g., lignin and/or extractives. Moreover, the intensity may also be influenced by sample spatial heterogeneity, as the Raman signal may be weaker in endosperm pores. Furthermore, the map's white points correspond to outlier spectra identified by PCA and removed from the dataset.

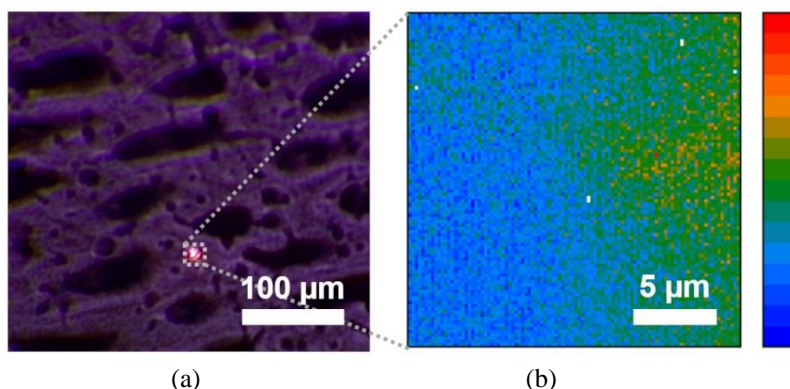


Figure 5. (a) Optical microscopy image of 785 nm laser-focused on a plasma-treated sample surface. (b) Average intensity map for Raman imaging of 20 x 20 μm^2 region analyzed in a plasma-treated sample.

Figure 6 shows average Raman spectra for plasma-treated samples compared to the untreated sample, analyzed at the same conditions. The Raman spectrum of both samples presented several peaks found in reference spectra for xylan-type polysaccharides (1020, 1244, 1308, and 1360 cm^{-1}) [44,45]. These peaks may also be associated with mannan, as 1080, 1106, and 1133 cm^{-1} peaks were previously attributed to β -mannose units [46,47]. In particular, the 1106 cm^{-1} peak could also be associated with glucose units. In addition to the 1450 cm^{-1} peak, it may indicate cellulose presence [48]. Besides, the 1133 and 1465 cm^{-1} peaks could also be associated with epicuticular waxes [49–51].

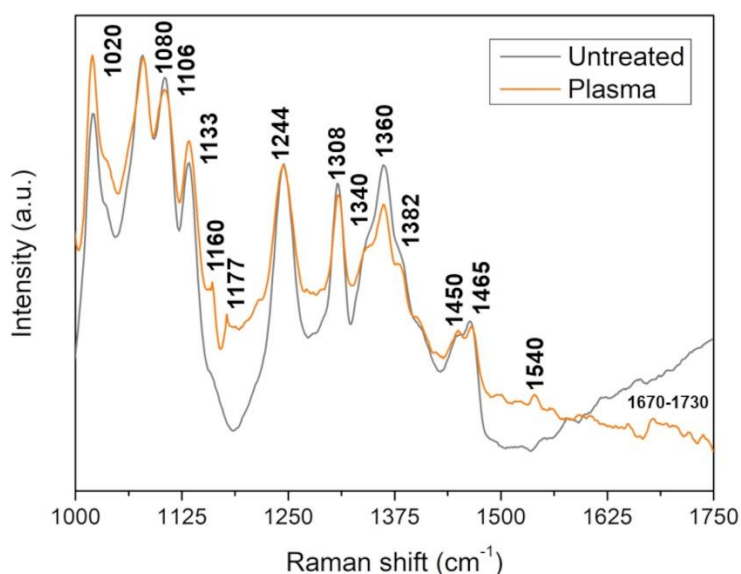


Figure 6. Average Raman spectra in 1000 to 1750 cm^{-1} range for untreated and plasma-treated samples.

An overall increase in background signal can be observed after plasma treatment, indicating that fluorescent substances such as lignin and extractives possess higher vibrational freedom or present an increased concentration at the sample surface [43]. Besides, the intensity of the 1020 and 1133 cm^{-1} peaks was increased compared to the 1080 cm^{-1} peak, while the 1360 cm^{-1} peak intensity was considerably decreased. Specifically, the 1020 cm^{-1} peak was assigned as CC and COH stretching in β -1,3-xylan, and the 1133 cm^{-1} peak corresponds to glycosidic linkages in β -1,4-xylan. In turn, the 1360 cm^{-1} peak was assigned as CH and OH bending in C(3)-OH from β -1,4-xylan [44]. As the hydroxyl at C(3) in the xylan molecule is a side group, these results indicate that the endosperm's polysaccharides present less vibrational freedom after plasma treatment, probably associated with the crosslinking promoted by plasma species. Besides, the opposite effect was observed for 1,3- β -linked xylan molecules, indicating that these polysaccharides in ivory nut endosperm are distinctly affected by the plasma treatment. These results will be further discussed alongside principal component analysis.

The decrease in 1360 cm^{-1} peak intensity may also have evidenced the 1340 and 1382 cm^{-1} peaks, present as shoulders in the untreated sample spectrum. These peaks were also attributed to xylan and correspond to vibrations with low Raman activity [44]. Besides, a relatively low-intensity peak could be observed at 1540 cm^{-1} , indicating the presence of carotenoids [52]. Other low-intensity contributions could be observed at 1160 and 1177 cm^{-1} , probably associated with epicuticular wax [49,51]. Moreover, several low-intensity peaks could be observed at the 1670-1730 cm^{-1} region, which could be attributed to carboxylic acids from extractives and C=O stretching from wax [49]. These results indicate the enrichment of sample surfaces with hydrophobic waxes and other extractive substances, which may be initially present in endosperm pores. However, except for peaks associated with xylan, these substances presented subtle contributions to the Raman spectra, and their concentrations may vary over the sample surface. Hence, the principal analysis was performed on Raman imaging data to highlight features with weak spectral contributions.

3.4. Principal component analysis of Raman imaging data.

Average intensity score maps for plasma-treated samples are shown in Figure 7, containing results for the first four principal components. The scores map for PC1 presented a similar aspect to the average map observed in Figure 5. As the loadings spectrum (Figure 8) appears to be associated with an average signal with no negative correlations, the variation observed in the PC1 map may be associated with topography. The region colored in red may be higher than the blue region due to the higher accumulation of crosslinked material on the surface.

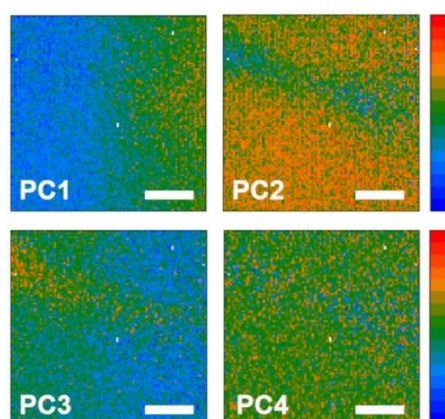


Figure 7. Average intensity score maps for the first four principal components—scale bars = 5 μm .

On the other hand, PC2 distinguishes between the bulk of the endosperm (red) and a tubule (blue). This component's spectral loadings presented a strong influence of background signal, indicating that fluorescent substances are accumulated in the endosperm tubules.

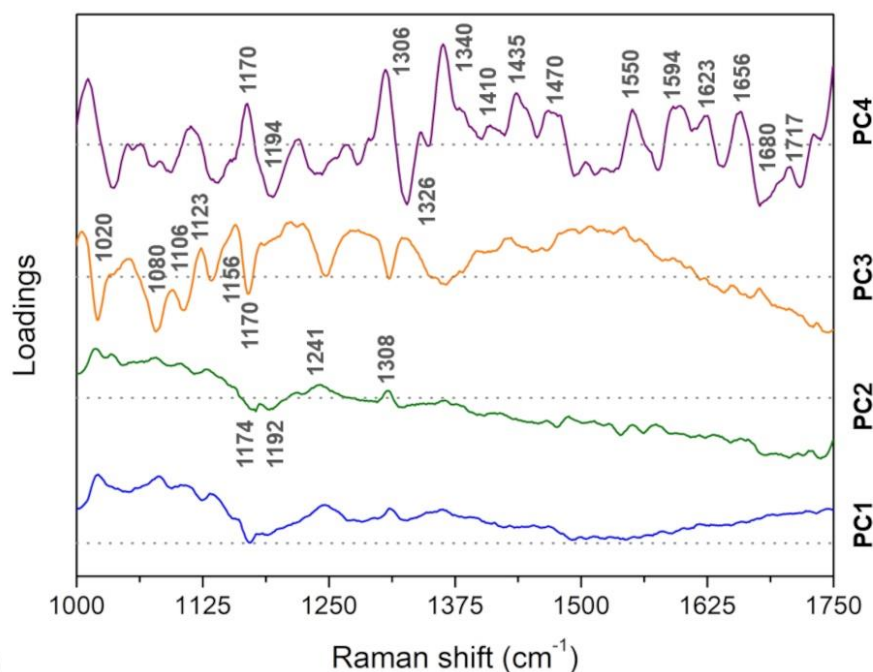


Figure 8. Spectral loadings for the first four principal components.

The third principal component's scores map also distinguishes the material accumulated in the pores from the endosperm bulk's surface. The negatively correlated region (blue) is associated with contributions from xylan (1020, 1080, 1106, and 1170 cm^{-1}), while the 1170 cm^{-1} peak was attributed to epicuticular wax [44,51]. In turn, the positively correlated region, corresponding to the endosperm pores, also presented a contribution from xylan (1020 cm^{-1}) and a peak at 1156 cm^{-1} . During Raman characterization of sorghum epicuticular waxes, Farber *et al.* (2019) found that intact wax presented a peak at 1170 cm^{-1} that was shifted to 1156 cm^{-1} after extraction with chloroform [51]. Thus, the presence of 1156 and 1170 cm^{-1} contributions in distinct regions evidence the effect of plasma treatment on wax structure and indicates its migration and crosslinking on the surface. The other peaks present in the spectra are broad, and intensity was influenced by fluorescence background; thus, they were not considered in this discussion.

PC4 scores map presented a similar aspect to the observed phase contrast in Figure 4. Positively and negatively correlated regions are distributed all over the surface, in a similar way to the stiffer and softer regions observed by AFM. Besides, the spectral loadings are not as influenced by the fluorescence background as the first components. This principle component appeared to distinguish the extractive substances presented as a repolymerized layer on the surface. For instance, the negatively correlated loadings presented contributions from carboxylic acid groups (1680 cm^{-1}), C=O stretching (1717 cm^{-1}), aliphatic OH bending (1326 cm^{-1}) and phenol groups (1194 cm^{-1}) [49,53]. These findings demonstrate the higher concentration of polar extractive substances in the blue regions of the scores map. In turn, the positively correlated loadings presented contributions from waxes (1170, 1410, 1435 and 1470 cm^{-1}), xylan (1306 and 1340 cm^{-1}) and lignin (1594, 1623 and 1656 cm^{-1}) [44,51,53]. These results indicate that plasma treatment induces the formation of an extractives-derived

layer on the sample surface containing regions abundant in hydrophobic waxes associated with xylan and lignin. These cell wall constituents may be previously accumulated in the endosperm pores before treatment. Notably, a few xylan peaks could also be found in reference spectra for mannose units [46,47]. Hence, xylan's peaks could also be associated with mannan, which is widely reported as the main constituent of ivory nut endosperm.

4. Conclusions

Surface modification of ivory nut endosperm by an atmospheric air plasma jet promoted surface hydrophobization. This result was attributed to the migration and repolymerization of extractives and cell wall polymers on the sample surface, forming a chemically heterogeneous layer containing polar substances, hydrophobic waxes, mannan, xylan, and lignin. These compounds may be natively present in the endosperm pores as reserve and defense substances. Our results demonstrate that plasma modification of seeds may be affected by the energetic species present in the plasma discharge and by chemical and structural factors such as extractives content and porosity, respectively.

Funding

This research was funded by CNPq (Conselho Nacional de Desenvolvimento Científico e Tecnológico) and was financed in part by the Coordenação de Aperfeiçoamento de Pessoal de Nível Superior – Brasil (CAPES) – Finance Code 001.

Acknowledgments

The authors would like to acknowledge the infrastructure and support from the Department of Metallurgical and Materials Engineering (DMM/PEMM/COPPE) from the Federal University of Rio de Janeiro (UFRJ).

Conflicts of Interest

The authors declare no conflict of interest. The funders had no role in the design of the study; in the collection, analyses, or interpretation of data; in the writing of the manuscript, or in the decision to publish the results.

References

1. Sonego, M.; Fleck, C.; Pessan, L.A. Mesocarp of Brazil nut (*Bertholletia excelsa*) as inspiration for new impact resistant materials, *Bioinspir. Biomim.* **2019**, *14*, 1-15, <https://doi.org/10.1088/1748-3190/ab2298>.
2. Nam, H.C.; Park, W.H. Eco-friendly poly(lactic acid) microbeads for cosmetics via melt electrospraying, *Int. J. Biol. Macromol.* **2020**, *157*, 734-742, <https://doi.org/10.1016/j.ijbiomac.2019.11.240>.
3. Schmier, S.; Hosoda, N.; Speck, T. Hierarchical structure of the *Cocos nucifera* (coconut) endocarp: Functional morphology and its influence on fracture toughness, *Molecules* **2020**, *25*, 1-19, <https://doi.org/10.3390/molecules25010223>.
4. Pellis, A.; Malinconico, M.; Guarneri, A.; Gardossi, L. Renewable polymers and plastics: Performance beyond the green. *N. Biotechnol.* **2021**, *60*, 146-158, <https://doi.org/10.1016/j.nbt.2020.10.003>.
5. Llanes, L.; Dubessay, P.; Pierre, G.; Delattre, C.; Michaud, P. Biosourced Polysaccharide-Based Superabsorbents. *Polysaccharides* **2020**, *1*, 51-79, <https://doi.org/10.3390/polysaccharides1010005>.
6. Brokamp, G.; Borgtoft Pedersen, H.; Montúfar, R.; Jácome, J.; Weigend, M.; Balslev, H. Productivity and management of *Phytelephas aequatorialis* (Arecaceae) in Ecuador. *Ann. Appl. Biol.* **2014**, *164*, 257-269.
7. Barfod, A.S. The rise and fall of vegetable ivory. *Principes* **1989**, *33*, 181-190.
8. Sosa export, Tagua Microbeads. Available online: <https://sosa-export.com/tagua-white-exfoliant/>, accessed on 28 September 2020.

9. Trafino, Tagua Natural White Exfoliant. Available online: <https://trafino.net/tagua-for-a-responsible-sustainable-cosmetics-industry/>, accessed on 28 September 2020.
10. Yang, W.; Jung, J.-Y.; Meyers, M.A.; Wang, A.; Chu, B.Y.; Coimbra, C.F.M. A Sustainable Substitute for Ivory: the Jarina Seed from the Amazon. *Sci. Rep.* **2015**, *5*, 1–10, <https://doi.org/10.1038/srep14387>.
11. Ferreira da Silva, Y.; Queiroz, V. de M.; Kling, I.C.S.; Archanjo, B.S.; Oliveira, R.N.; Simao, R.A. Antibacterial coatings on vegetable ivory obtained by cold plasma jet activation of silicone and copaiba oils. *Plasma Process. Polym.* **2020**, *17*, 1–15, <https://doi.org/10.1002/ppap.202000035>.
12. Ghysels, S.; Estrada León, A.E.; Pala, M.; Schoder, K.A.; Van Acker, J.; Ronsse, F. Fast pyrolysis of mannan-rich ivory nut (*Phytelephas aequatorialis*) to valuable biorefinery products. *Chem. Eng. J.* **2019**, *373*, 446–457, <https://doi.org/10.1016/j.cej.2019.05.042>.
13. González-Pérez, S.E.; de Robert, P.; Coelho-Ferreira, M. Seed Use and Socioeconomic Significance in Kayapó Handicrafts: A Case Study from Pará State, Brazil. *Econ. Bot.* **2013**, *67*, 1–16, <https://doi.org/10.1007/s12231-013-9220-0>.
14. Benchimol, R.L. *Patologia de sementes de espécies florestais na Amazônia*. **2000**.
15. Hon, D.N.S. *Chemical Modification of Lignocellulosic Materials*. 1st ed.; Routledge: New York, United States, **2017**.
16. Chauhan, P.S.; Puri, N.; Sharma, P.; Gupta, N. Mannanases: Microbial sources, production, properties and potential biotechnological applications. *Appl. Microbiol. Biotechnol.* **2012**, *93*, 1817–1830, <https://doi.org/10.1007/s00253-012-3887-5>.
17. Timell, T.E. Vegetable Ivory as a Source of a Mannan Polysaccharide. *Can. J. Chem.* **1957**, *35*, 333–338, <https://doi.org/10.1139/v57-048>.
18. Chanzy, H.; de Petkowicz, C.O.; Taravel, F.R.; Vuong, R.; Reicher, F. Linear mannan in the endosperm of *Schizolobium amazonicum*. *Carbohydr. Polym.* **2002**, *44*, 107–112, [https://doi.org/10.1016/S0144-8617\(00\)00212-5](https://doi.org/10.1016/S0144-8617(00)00212-5).
19. Grimaud, F.; Pizzut-Serin, S.; Tarquis, L.; Ladevèze, S.; Morel, S.; Putaux, J.L.; Potocki-Veronese, G. In Vitro Synthesis and Crystallization of β -1,4-Mannan. *Biomacromolecules* **2019**, *20*, 846–853, <https://doi.org/10.1021/acs.biomac.8b01457>.
20. Randeniya, L.K.; De Groot, G.J.J.B. Non-Thermal Plasma Treatment of Agricultural Seeds for Stimulation of Germination, Removal of Surface Contamination and Other Benefits: A Review. *Plasma Process. Polym.* **2015**, *12*, 608–623, <https://doi.org/10.1002/ppap.201500042>.
21. Attri, P.; Ishikawa, K.; Okumura, T.; Koga, K.; Shiratani, M. Plasma agriculture from laboratory to farm: A review. *Processes* **2020**, *8*, <https://doi.org/10.3390/PR8081002>.
22. Kang, M.-H.; Veerana, M.; Eom, S.; Uhm, H.-S.; Ryu, S.; Park, G. Plasma mediated disinfection of rice seeds in water and air. *J. Phys. D. Appl. Phys.* **2020**, *53*, <https://doi.org/10.1088/1361-6463/ab79de>.
23. Scholtz, V.; Pazlarova, J.; Souskova, H.; Khun, J.; Julak, J. Nonthermal plasma - A tool for decontamination and disinfection. *Biotechnol. Adv.* **2015**, *33*, 1108–1119, <https://doi.org/10.1016/j.biotechadv.2015.01.002>.
24. Fridman, A.A. *Plasma chemistry*. 1st ed.; Cambridge University Press: New York, United States, **2008**.
25. Ito, M.; Oh, J.S.; Ohta, T.; Shiratani, M.; Hori, M. Current status and future prospects of agricultural applications using atmospheric-pressure plasma technologies. *Plasma Process. Polym.* **2018**, *15*, <https://doi.org/10.1002/ppap.201700073>.
26. Múgica-Vidal, R.; Sainz-García, E.; Álvarez-Ordóñez, A.; Prieto, M.; González-Raurich, M.; López, M.; López, M.; Rojo-Bezares, B.; Sáenz, Y.; Alba-Elías, F. Production of Antibacterial Coatings Through Atmospheric Pressure Plasma: a Promising Alternative for Combatting Biofilms in the Food Industry. *Food Bioprocess Technol.* **2019**, *12*, 1251–1263, <https://doi.org/10.1007/s11947-019-02293-z>.
27. Feizollahi, E.; Misra, N.N.; Roopesh, M.S. Factors influencing the antimicrobial efficacy of Dielectric Barrier Discharge (DBD) Atmospheric Cold Plasma (ACP) in food processing applications. *Crit. Rev. Food Sci. Nutr.* **2020**, 1–24, <https://doi.org/10.1080/10408398.2020.1743967>.
28. Profili, J.; Asadollahi, S.; Vinchon, P.; Dorris, A.; Beck, S.; Sarkassian, A.; Stafford, L. Recent progress on organosilicon coatings deposited on bleached unrefined Kraft paper by non-thermal plasma process at atmospheric pressure. *Prog. Org. Coatings* **2020**, *147*, <https://doi.org/10.1016/j.porgcoat.2020.105865>.
29. Fanelli, F.; Fracassi, F. Atmospheric pressure non-equilibrium plasma jet technology: general features, specificities and applications in surface processing of materials. *Surf. Coatings Technol.* **2017**, *322*, 174–201, <https://doi.org/10.1016/j.surfcoat.2017.05.027>.
30. Lu, X.; Naidis, G.V.; Laroussi, M.; Reuter, S.; Graves, D.B.; Ostrikov, K. Reactive species in non-equilibrium atmospheric-pressure plasmas: Generation, transport, and biological effects. *Phys. Rep.* **2016**, *630*, 1–84, <https://doi.org/10.1016/j.physrep.2016.03.003>.
31. Khamsen, N.; Onwimol, D.; Teerakawanch, N.; Dechanupaprittha, S.; Kanokbannakorn, W.; Hongesombut, K.; Srisophon, S. Rice (*Oryza sativa* L.) Seed Sterilization and Germination Enhancement via Atmospheric Hybrid Nonthermal Discharge Plasma. *ACS Appl. Mater. Interfaces* **2016**, *8*, 19268–19275, <https://doi.org/10.1021/acsami.6b04555>.
32. Kawakami, R.; Yoshitani, Y.; Mitani, K.; Niibe, M.; Nakano, Y.; Azuma, C.; Mukai, T. Effects of air-based nonequilibrium atmospheric pressure plasma jet treatment on characteristics of polypropylene film surfaces. *Appl. Surf. Sci.* **2020**, *509*, <https://doi.org/10.1016/j.apsusc.2019.144910>.

33. Kondeti, V.S.S.K.; Zheng, Y.; Luan, P.; Oehrlein, G.S.; Bruggeman, P.J. O₂·H₂O·OH radical etching probability of polystyrene obtained for a radio frequency driven atmospheric pressure plasma jet. *J. Vac. Sci. Technol. A* **2020**, *38*, <https://doi.org/10.1116/6.0000123>.
34. Vesel, A.; Zaplotnik, R.; Primc, G.; Mozetič, M. Evolution of the surface wettability of PET polymer upon treatment with an atmospheric-pressure plasma jet. *Polymers (Basel)* **2020**, *12*, <https://doi.org/10.3390/polym12010087>.
35. Beleites, C.; Sergo, V. hyperSpec: a package to handle hyperspectral data sets in R. Available online: <https://github.com/cbeleites/hyperSpec>, accessed on 28 September **2020**.
36. Bonifacio, A.; Beleites, C.; Vittur, F.; Marsich, E.; Semeraro, S.; Paoletti, S.; Sergo, V. Chemical imaging of articular cartilage sections with Raman mapping, employing uni- and multi-variate methods for data analysis. *Analyst* **2010**, *135*, 3193–3204, <https://doi.org/10.1039/c0an00459f>.
37. Žigon, J.; Petrič, M.; Dahle, S. Dielectric barrier discharge (DBD) plasma pretreatment of lignocellulosic materials in air at atmospheric pressure for their improved wettability: a literature review. *Holzforschung* **2018**, *72*, 979–991, <https://doi.org/10.1515/hf-2017-0207>.
38. Busnel, F.; Blanchard, V.; Prigent, J.; Stafford, L.; Riedl, B.; Blanchet, P.; Sarkissian, A. Modification of Sugar Maple (*Acer saccharum*) and Black Spruce (*Picea mariana*) Wood Surfaces in a Dielectric Barrier Discharge (DBD) at Atmospheric Pressure. *J. Adhes. Sci. Technol.* **2010**, *24*, 1401–1413, <https://doi.org/10.1163/016942410X501007>.
39. Šernek, M.; Kamke, F.A.; Glasser, W.G. Comparative analysis of inactivated wood surfaces. *Holzforschung* **2004**, *58*, 22–31, <https://doi.org/10.1515/HF.2004.004>.
40. Chanzy, H.D.; Grosrenaud, A.; Vuong, R.; Mackie, W. The crystalline polymorphism of mannan in plant cell walls and after recrystallisation. *Planta* **1984**, *161*, 320–329, <https://doi.org/10.1007/BF00398722>.
41. Scholz, I.; Buckins, M.; Dolge, L.; Erlinghagen, T.; Weth, A.; Hischen, F.; Mayer, J.; Hoffmann, S.; Riederer, M.; Riedel, M.; Baumgartner, W. Slippery surfaces of pitcher plants: *Nepenthes* wax crystals minimize insect attachment via microscopic surface roughness. *J. Exp. Biol.* **2010**, *213*, 1115–1125, <https://doi.org/10.1242/jeb.035618>.
42. Colares, C.J.G.; Pastore, T.C.M.; Coradin, V.T.R.; Camargos, J.A.A.; Moreira, A.C.O.; Rubim, J.C.; Braga, J.W.B. Exploratory analysis of the distribution of lignin and cellulose in woods by Raman imaging and chemometrics. *J. Braz. Chem. Soc.* **2015**, *26*, 1297–1305, <https://doi.org/10.5935/0103-5053.20150096>.
43. Lähdetie, A.; Nousiainen, P.; Sipilä, J.; Tamminen, T.; Jääskeläinen, A.S. Laser-induced fluorescence (LIF) of lignin and lignin model compounds in Raman spectroscopy. *Holzforschung* **2013**, *67*, 531–538, <https://doi.org/10.1515/hf-2012-0177>.
44. Kačuráková, M.; Wellner, N.; Ebringerová, A.; Hromádková, Z.; Wilson, R.H.; Belton, P.S. Characterisation of xylan-type polysaccharides and associated cell wall components by FT-IR and FT-Raman spectroscopies. *Food Hydrocoll.* **1999**, *13*, 35–41, [https://doi.org/10.1016/S0268-005X\(98\)00067-8](https://doi.org/10.1016/S0268-005X(98)00067-8).
45. Zeng, Y.; Yarbrough, J.M.; Mittal, A.; Tucker, M.P.; Vinzant, T.B.; Decker, S.R.; Himmel, M.E. In situ label-free imaging of hemicellulose in plant cell walls using stimulated Raman scattering microscopy. *Biotechnol. Biofuels* **2016**, *9*, <https://doi.org/10.1186/s13068-016-0669-9>.
46. Arboleda, P.H.; Loppnow, G.R. Raman spectroscopy as a discovery tool in carbohydrate chemistry. *Anal. Chem.* **2000**, *72*, 2093–2098, <https://doi.org/10.1021/ac991389f>.
47. Gelder, J. De; Gussem, K. De; Vandenabeele, P.; Moens, L. Reference database of Raman spectra of biological molecules. **2007**, 1133–1147.
48. Lupoi, J.S.; Gjersing, E.; Davis, M.F. Evaluating lignocellulosic biomass, its derivatives, and downstream products with Raman spectroscopy. *Frontiers in Bioengineering and Biotechnology* **2015**, *3*, 1–18, <https://doi.org/10.3389/fbioe.2015.00050>.
49. Mateu, B.P.; Hauser, M.T.; Heredia, A.; Gierlinger, N. Waterproofing in *Arabidopsis*: Following phenolics and lipids in situ by Confocal Raman Microscopy. *Front. Chem.* **2016**, *4*, 1–13, <https://doi.org/10.3389/fchem.2016.00010>.
50. Czamara, K.; Majzner, K.; Pacia, M.Z.; Kochan, K.; Kaczor, A.; Baranska, M. Raman spectroscopy of lipids: A review. *J. Raman Spectrosc.* **2015**, *46*, 4–20, <https://doi.org/10.1002/jrs.4607>.
51. Farber, C.; Li, J.; Hager, E.; Chemelewski, R.; Mullet, J.; Rogachev, A.Y.; Kurouski, D. Complementarity of Raman and Infrared Spectroscopy for Structural Characterization of Plant Epicuticular Waxes. *ACS Omega* **2019**, *4*, 3700–3707, <https://doi.org/10.1021/acsomega.8b03675>.
52. Schulz, H.; Baranska, M.; Baranski, R. Potential of NIR-FT-Raman spectroscopy in natural carotenoid analysis. *Biopolymers* **2005**, *77*, 212–221, <https://doi.org/10.1002/bip.20215>.
53. Agarwal, U.P.; McSweeney, J.D.; Ralph, S.A. FT-raman investigation of milled-wood lignins: Softwood, hardwood, and chemically modified black spruce lignins. *J. Wood Chem. Technol.* **2011**, *31*, 324–344, <https://doi.org/10.1080/02773813.2011.562338>.